Poromechanical modelling of the time-dependent response of *in vivo* human skin during extension

Thomas Lavigne[a,b,c], Stéphane Urcun[a], Emmanuelle Jacquet[d], Jérôme Chambert[d], Aflah Elouneg[d], Camilo A. Suarez-Afanador[a], Stéphane P. A. Bordas[a], Giuseppe Sciumè[c,e], Pierre-Yves Rohan*[b,e]

[a] *Institute of Computational Engineering, Department of Engineering, University of Luxembourg, 2 place de l'université, Esch-sur-Alzette, L-4365, Luxembourg*
[b] *Institut de Biomécanique Humaine Georges Charpak, Arts et Métiers Institute of Technology, 151 boulevard de l'hôpital, Paris, F-75013, France*
[c] *CNRS, Bordeaux INP, I2M, UMR 5295, I2M Bordeaux, Arts et Metiers Institute of Technology, University of Bordeaux, Talence, F-33400, France*
[d] *Université Marie et Louis Pasteur, CNRS, institut FEMTO-ST, Besancon, F-25000, France*
[e] *Institut Universitaire de France (IUF), Paris, France*

Abstract

This paper proposes a proof of concept application of a biphasic constitutive model to identify the mechanical properties of *in vivo* human skin under extension. Although poromechanics theory has been extensively used to model other soft biological tissues, only a few studies have been published for skin, and most have been limited to *ex vivo* or *in silico* conditions. However, *in vivo* procedures are crucial to determine the subject-specific properties at different body sites. This study focuses on cyclic uni-axial extension of the upper arm skin, using unpublished data collected by Chambert et al. Our analysis shows that a two-layer finite element model allows representing all relevant features of the observed mechanical response to the imposed external loading, which was composed, in this contribution, of four loading-sustaining-unloading cycles. The Root Mean Square Error (RMSE) between the calibrated model and the measured Force-time response was 8.84×10^{-3} N. Our biphasic model represents a preliminary step toward investigating the mechanical conditions responsible for the onset of injury. It

*Corresponding author
Email address: pierre-yves.rohan@ensam.eu (Pierre-Yves Rohan*)

July 15, 2025

allows for the analysis of changes in Interstitial Fluid (IF) pressure, flow, and osmotic pressure, in addition to the mechanical fields. Future work will focus on the interaction of multiple biochemical factors and the complex network of regulatory signals.

Keywords: Human skin, Poro-elasticity, Time-dependent, FEniCSx

1. Introduction

The skin is a multi-layered structure, the largest organ in the human body. It is vital for protecting the tissues from pollutants, bacterial infections, and sunlight. Knowledge of the ways the skin behaves under mechanical load is crucial for various applications such as skin surgery (Ogawa et al. [53]), diagnostic tools for skin pathology (Jasaitiene et al. [38]), design of medical devices or devices for personal care or trans-epidermal drug delivery with micro-needles or micro-jets (Waghule et al. [85]), and treatment monitoring of skin diseases (Dubois et al. [16]). Several *in vivo* measurement tests have been specifically designed to accurately determine the behaviour of skin tissues, such as the suction test (Alexander and Cook [2], Humbert et al. [35]), torsion test (Agache et al. [1], Humbert et al. [35]), compressive test (Oomens et al. [59, 55], Zhang et al. [92], Tran [79], Pailler-Mattéi and Zahouani [62], Bosboom et al. [7]), indentation test (Pailler-Mattéi and Zahouani [62]), and longitudinal extension test (Humbert et al. [35], Khatyr et al. [43]).

In particular, these studies considered a broad spectrum of models and have shown the strain rate dependency of skin mechanical properties (Humbert et al. [35], Eshel and Lanir [20], Shergold et al. [71]). Yet, attempts to characterise the time-dependence of the mechanical response of skin tissue to external loading generally assume a viscoelastic formulation (Flynn et al. [22], Gerhardt et al. [26]). These models ignore the structural bi-phasic nature of the tissue.

Poroelastic constitutive models have been proposed as an alternative to viscoelastic models to capture the time-dependent response of soft tissues. Initially introduced for soil mechanics, these models are largely used in biomechanics. They allow the coupling of the solid behaviour of a scaffold with the fluid mechanics of one or more fluids saturating the solid medium and have been adapted to the biomechanical field(Argoubi and Shirazi-Adl [4], Franceschini et al. [23], Sciumè et al. [69], Peyrounette et al. [64], Siddique et al.

[72], Gimnich et al. [28], Hosseini-Farid et al. [34]). Porous media models represent a promising approach for integrating multiscale/multiphysics data to probe biologically relevant phenomena at smaller scales and embed relevant mechanisms at larger scales. This is particularly the case with the interaction of multiple biochemical factors (enzymes, growth factors, hormones, proteins) and the complex network of regulatory signals, which determine tissue characteristics and their evolution in processes such as growth and remodelling (Eskandari and Kuhl [21]), ageing, and the onset of injuries such as pressure ulcers (Sree et al. [75], Gefen et al. [25]).

A number of research teams have proposed utilising this approach to characterise and model the mechanical response of various tissues, including the brain (Budday et al. [8], Hosseini-Farid et al. [34], Greiner et al. [29], Urcun et al. [81, 80], Hervas-Raluy et al. [32], Carrasco-Mantis et al. [10]), the liver (Ricken and Lambers [66]), the meniscus (Kazemi et al. [42], Uzuner et al. [84], Bulle [9], Uzuner et al. [83]), and muscle tissue (Lavigne et al. [45]). In these studies, the biological tissues were modelled as biphasic systems with the behaviour governed by the properties of the porous solid and the fluid occupying the pores. This was based on the balance of mass and momentum conservation equations.

Although the theory of poromechanics has been extensively applied in other soft biological tissues, only a few studies have been published for skin, and these were limited to *in silico* and *ex vivo* studies.

One of the first contributions was made by (Oomens et al. [54]). The authors developed a poroelastic model of the skin based on the large strain theory, using a hyper-elastic (Tong and Fung [78]) constitutive model for the solid phase and a nonlinear strain-dependent permeability. The model was implemented in a Finite Element model to simulate the quasi-static indentation response of *ex vivo* porcine skin (Oomens et al. [56]). More recently, Weir Weiss et al. [88] developed a custom setup to apply a pressure-driven fluid flow across skin tissues. The resulting flow rate and cross-sectional image acquisition by optical coherence tomography (OCT) combined with digital image correlation (DIC) were used to calculate the internal strains within the tissue and to characterise ex vivo local strain and permeability of porcine skin tissue under compression loading. Likewise, Wahlsten et al. [87] analysed the mechanical behaviour of skin from the cellular to the tissue length scale through dedicated experiments to resolve these discrepancies. Of particular interest, the same team also conducted uni-axial monotonic, cyclic, and relaxation experiments on a total of 37 human and 33 Murine

skin samples (Wahlsten et al. [86]). They showed that skin volume is significantly reduced due to tensile elongation. However, the loading was not controlled and applied by a human operator. To the best of the authors' knowledge, little application of biphasic constitutive modelling of the skin *in vivo* has been proposed. Yet, the development of *in vivo* procedures is crucial to determine subject-specific properties at different body sites given different loading conditions.

In this study, we focus on the cyclic uni-axial extension of the upper arm skin from unpublished data previously collected by Chambert et al. under conditions similar to those described in Chambert et al. [11]. The relaxation phenomenon observed in this experiment is of great interest to the poromechanical approach. Indeed, poromechanics takes into account the pressurisation of interstitial fluid in the different layers of the skin, which makes an important contribution to this relaxation during sustained tensile loading.

The experimental data are presented followed by the poromechanical model. The values of the parameters are then discussed based on the physiological and modelling literature. The process of identifying the physical parameters is explained and the numerical response of the model over time is shown. This study is an encouraging step towards the use of poromechanics for *in vivo* skin modelling. The authors hope that it will encourage experimentalists to improve their experimental protocols and measure other quantities (e.g. fluid pressures, fluid flows) further to test the reliability of porous media modelling approaches.

2. Materials and methods

2.1. Portable extensometer description

A portable in-house extensometer (Figure 1) has been used to perform an uniaxial in vivo tensile test while limiting disturbances from the skin surrounding the region of interest (Jacquet et al. [37, 36], Chambert et al. [11]). The portable extensometer consists essentially of an electric motor, two guiding pillars and two double pads and a rectangular frame. The two double pads, one fixed to the frame and the other one is actuated by an electrical motor, allow for the application of imposed displacement to the skin. Each double pad, made up of a central pad (also called measuring pad) surrounded by a 'U-shaped' guarding pad, is assumed to be rigidly attached to the skin surface by means of an adhesive used in dermatological surgery.

The pads are initially separated by a length of $L_0 = 36$ mm. The LVDT displacement sensor provides the position of the mobile pad. The force sensor is a bronze-beryllium cantilever beam equipped with strain gauges stuck on the sensor. The measured reaction force corresponds to the force applied to the central pad. A detailed description of the experimental device can be found in Jacquet et al. [37].

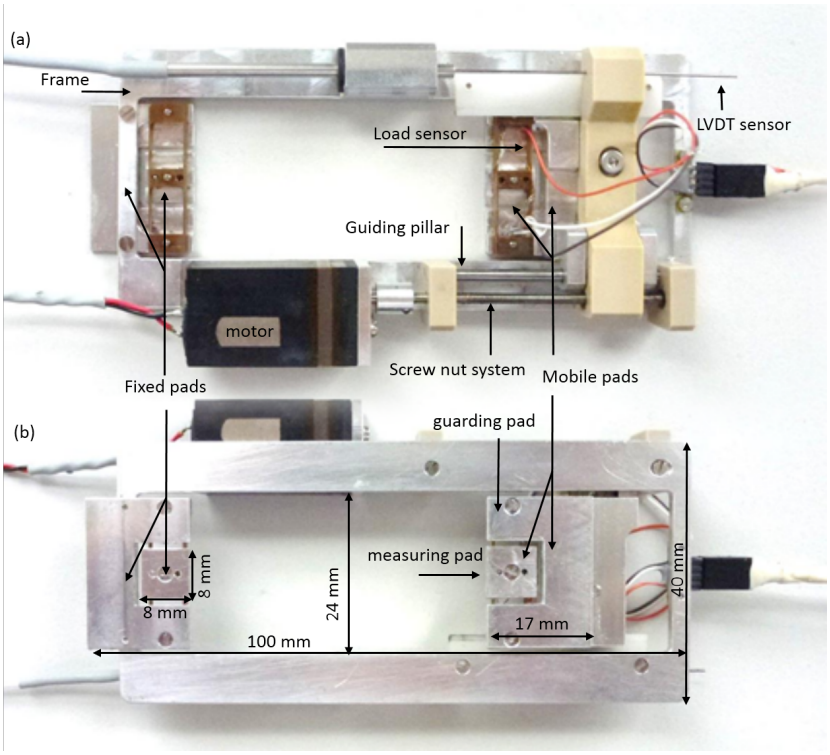

Figure 1: Portable extensometer: (a) top view; (b) bottom view (from Jacquet et al. [37] with permission).

2.2. Data Acquisition

Using an ultra-light, in-house portable extensometer described in Jacquet et al. [37], Chambert et al. have carried out, in accordance with ethical standards as set out by institutional and national committee and with the Helsinki Declaration of 1975, as revised in 2000, uni-axial extension measurements on the left upper arm (dorsal aspect) of a 22-year-old female. Identification of participants has been made anonymous for the publication

of this article. The extensometer is a prototype consisting of two sets of square pads: one static and one mobile. Each set includes a central pad, where measurements are taken, and a surrounding 'U-shaped' guarding pad. The guarding pad is designed to minimize disturbances from the surrounding skin in the region of interest by applying the same extension to the neighbouring skin, thereby ensuring uni-axial extension. Further details about the device, along with images of the extensometer, can be found in Jacquet et al. [36, 37] and Chambert et al. [11].

During this experimental campaign, four loading-sustaining-unloading repetitions (relaxation tests) were performed at a controlled speed of 1 mm s^{-1} to exhibit the time-dependent properties (Figure 2). The unloading-loading step between the third and fourth cycles was made slightly different, and the real displacement was recorded all along the experiment using a LVDT sensor, providing the exact loading.

The reaction force was monitored every 0.01 s, and the maximum applied displacement was set to 9.45 mm (Figure 2). This reaction force corresponds to the difference between the current stress state and the pre-stressed state of the skin. The initial negative reaction force (and the resulting force after unloading) is believed to arise from the installation of the extensometer on the skin. This can be likened to a pre-stress state, which is discussed in the section 4. All measurements have been made in temperature and hygrometry-regulated rooms (20–22°C, 40–60% relative humidity) after a rest time of 20 min. The experimental data is accessible in the github as supplementary material.

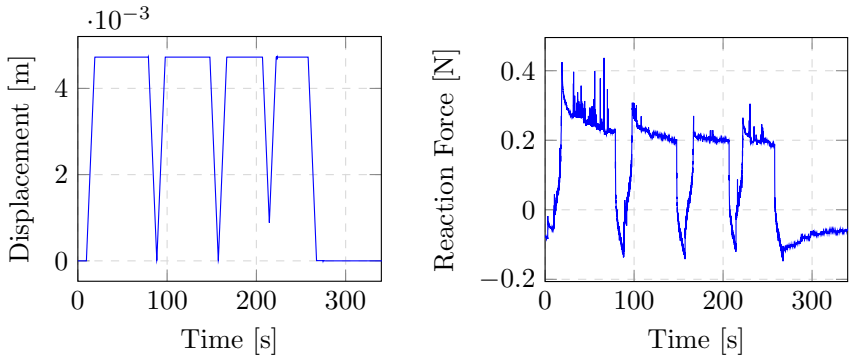

Figure 2: Imposed displacement (half of the displacement extracted from the LVDT sensor for symmetry purpose in the model) and resulting reaction force.

2.3. Geometrical modelling

Two curved layers were considered, namely the cutis (composed of the epidermis and the dermis) and the subcutis (defined as the hypodermis) (Figure 3). The model is a low fidelity bilayered model assuming only different material properties without relative displacement between the layers. Therefore we assume that the cutis and the subcutis are strongly related and displace together at the interface, including stress continuity.

Before the experiment, an echography was performed on the dorsal upper arm using a commercial device (Aixplorer, SuperSonic Imagine, France) with a linear ultrasound probe of 8 MHz central frequency (SuperLinear SL 15-4). The echography parameters used in this study did not permit the identification of the subcutis boundaries, so the image was utilised solely to measure the thickness of the cutis. A thickness of approximately 2 mm was identified for the cutis, based on the image scale. The subcutis thickness was defined based on prior studies (Birkebaek et al. [6], Mellor et al. [51]). Therefore, a curved bi-layer geometry was considered with a thickness of 2 mm for the cutis and 8 mm for the subcutis. The radius was fixed to 48 mm according to the previous work of Elouneg [17], and based on the measured perimeter of the arm.

Considering the geometry and the boundary conditions (especially of the in-house extensometer geometry and the uni-axial aspect of the experiment), two axes of symmetry were introduced. The symmetries are represented by the harsh surfaces in Figure 3. A mesh of 11,310 tetrahedral elements was generated using the gmsh software (Geuzaine and Remacle [27]) and a local refinement close to the in-house device was performed. Given the strong compatibility between the gmsh and FEniCSx environments, the facets, as well as the elements, were tagged at this stage to apply the boundary conditions. The distances on the x- and y- directions were artificially increased to limit the risks of edge effects in the region of interest, *i.e.* the region covered by the in-house device.

Another refined mesh of 43,767 elements was also created to assess the trustworthiness of the computed fields. A root mean square error of 8.01×10^{-3} N was found between the resulting reaction forces obtained by the two meshes. This difference was deemed acceptable given the required increase in computation time which changed from 1h45min to 22h06min with the same configuration of the computer. Hence, the mesh of 11,310 elements was considered for this study.

2.4. Material modelling

During the experiment, the skin was stretched up to 25 %. This level of stretching goes beyond the hypothesis of small strains. Furthermore, previous studies highlighted the non-linear behaviour of the skin with its "J-shaped" stress-strain curve (Joodaki and Panzer [39], Yazdi and Baqersad [90]).

A poro-hyper-elastic model was therefore assumed to model the mechanical behaviour of skin tissue. Since the replicated experiment was uni-axial (and supposed to be aligned with the fibre direction of the dermis), for sake of simplicity, the material was assumed to be isotropic, whereas the skin response is known to be transversely isotropic (Elouneg et al. [18], Kalra and Lowe [41], Yazdi and Baqersad [90], Joodaki and Panzer [39], Annaidh et al. [3], Khatyr et al. [43]).

The model is based on the equations of mass and momentum conservation of the fluid and solid phases (Equations (1) and (2)) as described in Lavigne et al. [46]. The two phases considered in the model are: the solid phase (collagen-elastin matrix, structural cells), the fluid phase (interstitial fluid). The primary variables in the problem are the pressure in the interstitial space and the solid displacement (assuming the skin is saturated with a single fluid). Considering Ω_c for the cutis and Ω_s for the subcutis:

$$\left(\frac{\varepsilon_i^l}{K_i^l}+\frac{1-\varepsilon_i^l}{K_i^s}\right)\frac{\mathrm{D}^s p^l}{\mathrm{Dt}}+\nabla\cdot\mathbf{v}-\nabla\cdot\left(\frac{k_i^\varepsilon}{\mu^l}\nabla p^l\right)=0 \text{ on } \Omega_i,\ i\in[c,s], \quad (1)$$

$$\nabla\cdot\mathbf{t}^{\mathrm{tot}}=0 \text{ on } \Omega_i,\ i\in[c,s], \quad (2)$$

where $\frac{\mathrm{D}^s f}{\mathrm{Dt}}=\frac{\partial f}{\partial t}+\nabla f\cdot\mathbf{v}^s$ is the material derivative, $\varepsilon_i^l=\frac{\text{Liquid Volume}}{\text{Total Volume}}$ is the porosity of the medium, K_i^l and K_i^s respectively denotes the liquid and solid bulk moduli, p^l is the interstitial pressure, $\mathbf{v}$ is the solid velocity, k_i^ε corresponds to the intrinsic permeability, μ^l is the fluid viscosity, and $\mathbf{t}^{\mathrm{tot}}$ is the total stress tensor.

The total stress tensor is expressed as $\mathbf{t}^{\mathrm{tot}}=\mathbf{t}^{\mathrm{eff}}-\beta p^l\mathbf{I}_{\mathrm{d}}$, $\mathbf{t}^{\mathrm{eff}}$ being the effective stress in the sense of porous media mechanics, and assuming that the Biot coefficient (β) is close to one as typically done in biomechanics (Lavigne et al. [46]). This assumption results from a bulk modulus of the solid phase K_i^s largely higher than the overall bulk modulus of the porous scaffold (Sciumè [68]). To describe the solid behaviour, a Neo-Hookean hyper-elastic potential has been considered because of the straightforward relationship of its parameters (the Lamé coefficients by $\mu_i=\frac{E_i}{2(1-\nu_i)}$ and $\lambda_i=\frac{E_i\nu_i}{(1+\nu_i)(1-2\nu_i)}$ in

Ω_i) with the Young's modulus (E_i) and Poisson's ratio (ν_i). This choice was further supported by the ease of interpretation as such energy formulation allows for a direct evaluation of usual elastic parameters. Other strain-energy density functions (a comparison between strain-energy functions for the brain has been proposed in Budday et al. [8]) can be easily introduced in FEniCSx such as performed for the volumetric part in Lavigne et al. [46].

Let $\mathbf{F}$ denote the deformation gradient (Equation (3)), J, its determinant and $\mathbf{I}_\mathrm{d}$ the identity matrix.The deformation gradient $\mathbf{F}$ reads

$$\mathbf{F} = \mathbf{I}_\mathrm{d} + \nabla \mathbf{u}, \tag{3}$$

where $\mathbf{u}$ is the displacement of the solid phase.

From the deformation gradient $\mathbf{F}$, one can further introduce the right Cauchy-Green stress tensor $\mathbf{C}$ and its first invariant I_1 (Equations (4) and (5)).

$$\mathbf{C} = \mathbf{F}^\mathrm{T}\mathbf{F}, \tag{4}$$

$$I_1 = \mathrm{tr}(\mathbf{C}), \tag{5}$$

The theory of hyper-elasticity defines a potential of elastic energy $W(\mathbf{F})$ which can be expressed as the combination of an isochoric component and a volumetric component (Simo [73], Horgan and Saccomandi [33], Marino [50]).

$$W(\mathbf{F}) = \tilde{W}(I_1, J) + U(J), \tag{6}$$

where $\tilde{W}(I_1, J)$ is the isochoric part and $U(J)$ the volumetric one. A compressible formulation of the Neo-Hookean strain-energy potential from (Pence and Gou [63], Horgan and Saccomandi [33]) has been introduced as:

$$\tilde{W}(I_1, J) = \frac{\mu_i}{2}(I_1 - \mathrm{tr}(\mathbf{I}_\mathrm{d}) - 2\,\ln J), \tag{7}$$

The volumetric part proposed in Doll and Schweizerhof [15] has been adopted:

$$U(J) = \frac{K_i^s}{2}(\ln J)^2, \tag{8}$$

Finally, from the potential (Equation (6)) derives the first Piola-Kirchhoff stress tensor. Using Nanson's formula we obtain the effective Cauchy stress

such that:

$$\mathbf{t}^{\text{eff}} = J^{-1}\frac{\partial W}{\partial \mathbf{F}}\mathbf{F}^{T}, \tag{9}$$

A same constitutive law is introduced for the cutis (Ω_c) and the subcutis (Ω_s). To introduce the heterogeneity of the material parameters, they are mapped in the space within the considered finite element software FEniCSx. For the numerical introduction, please refer to the GitHub repository where the codes are made openly accessible and consult the tutorial by Lavigne et al. [46] for additional insights on implementing poromechanics in FEniCSx.

2.5. Boundary and Initial conditions

The poro-hyper-elastic problem is solved using a mixed space (Lavigne et al. [46]) allowing for the simultaneous solving of displacement (which typically represents the solid deformation) and pressure (which represents the fluid flow or pore pressure) within the same computational framework. Therefore, boundary conditions must be introduced for all the primary unknowns, namely the solid displacement of the scaffold and the interstitial pressure (Figure 3). The mesh not only covers the region of interest but has also been greatly increased to avoid side effects, therefore accounting for a no-flow condition at the boundaries (absence of leakage). No external forces were applied. The amplitude of the displacement applied to the model corresponds to the half of the effective displacement of the experiment recorded by the LVDT sensor. According to Elouneg et al. [18], the longitudinal displacement is linearly distributed along the central axis, with the displacement at the centre being half of that imposed on the moving pad. The displacement was applied to the patch and its guide pad (limiting rotational effects resulting from the orientation of the Langer lines in the skin). It is assumed that the mechanical problem can be addressed using two planes of symmetry (x, z) and (y, z) (Figure 3), although this approach does not fully capture the actual geometry and loading conditions. Dirichlet boundary conditions were also introduced on the symmetry planes and the vertical displacement of the bottom surface (Figure 3). The two other lateral surfaces were left free to deform to simulate semi-infinite boundary conditions, thereby reducing the risk of edge effects on the computed reaction force. Unlike the symmetry planes, adding Dirichlet boundary conditions was not considered appropriate, as no displacement measurements were taken outside of the ex-

tensometer. Imposing such conditions could have interfered with the "skin reorganisation" effect.

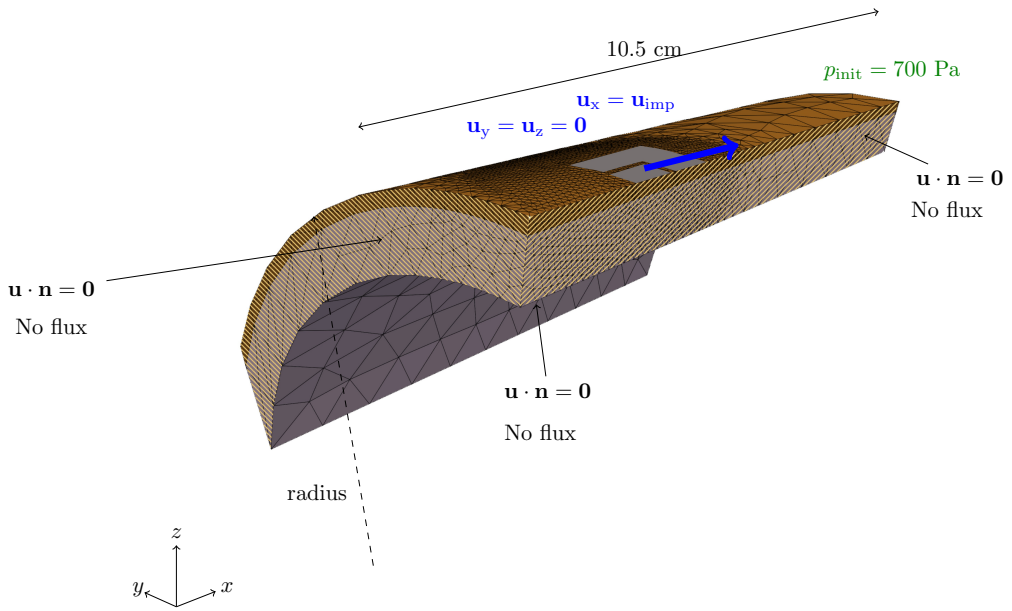

Figure 3: Mesh, boundary and initial conditions of the problem. The skin is assumed saturated by a single fluid. The initial pressure is set to 700 Pa to account for the homeostatic pressure. No flux is allowed on the external surfaces. Furthermore, two planes of symmetry are introduced ((x, z) and (y, z)) leading to a normal displacement imposed to zero ($\mathbf{u} \cdot \mathbf{n} = \mathbf{0}$). These are the hashed plans. The vertical displacement is blocked on the bottom surface. The other external surfaces are set free to move. The "u-shaped" patch and the patch itself (in gray) have an imposed displacement along the x-direction.

In the absence of experimental data regarding the *in vivo* pre-strain, no pre-stress nor pre-strain was introduced in the model. Regarding initial pressure of the interstitial fluid, experimental literature provides a wide range of physiological values: 2144 Pa for leg's subcutis, averaged from 19 healthy patients, in Hargens et al. [31]; from -670 to $+536$ Pa for palm hand's subcutis of 7 healthy patients, measured by two techniques, micro-puncture and wick-in-needle, in Wiig and Noddeland [89]. Additionally, repetitive measurements on pig's skin in Samant and Prausnitz [67], give the mean osmotic pressure of 725 Pa (this value is deduced from the increase of initial ionic strength of 4.03448 fold which provokes an increase of 2200 Pa of the homeostatic pressure). An initial guess of 700 Pa has been chosen, and the parameter has been included in the sensitivity analysis.

2.6. Calibration procedure

The poro-hyper-elastic model was implemented in the open-source environment FEniCSx. The implementation process is the same as the one developed in Lavigne et al. [46]. The corresponding codes are available on github (link here). To limit the effect of local minima during the calibration procedure, only the Young moduli and permeabilities were calibrated for each layer. The other parameters used were fixed according to the literature (see section 2.7). To support this choice, the Sobol' indices have been computed and results are reported in Appendix A.

A cost function based on the root mean square error (RMSE) of the reaction force (RF) was introduced (Equation (10)). The calibration was only performed in the first 145 seconds to assess the predictive potential of the model (Figure 4). Then, the identified parameters are used to model the full experiment. The cost function was only computed during the time steps of sustained load.

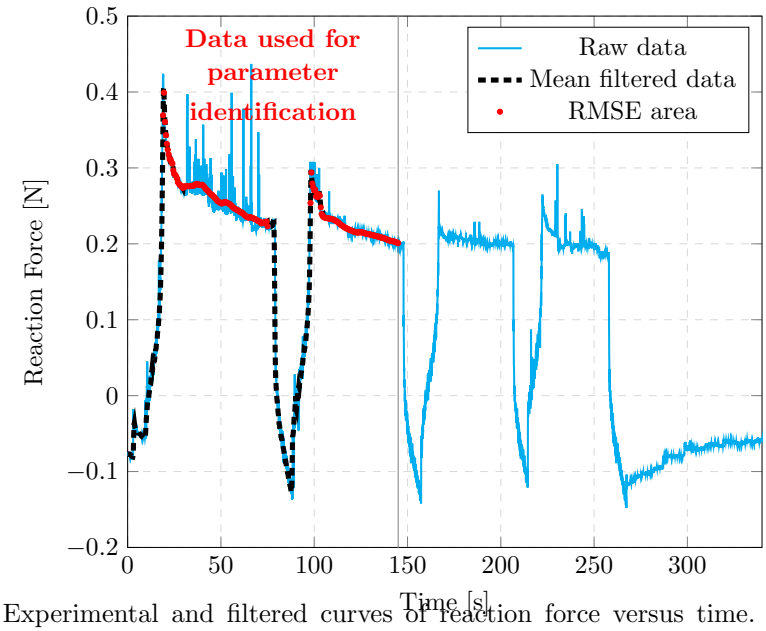

Figure 4: Experimental and filtered curves of reaction force versus time. Due to the presence of noise in the raw data (blue), the calibration area was first filtered (black dashed curve) and the cost function was only evaluated during the sustained displacement (red dots).

$$\text{RMSE} = \sqrt{\frac{\sum\limits_{t\in[20,\ 75]} (RF - RF_{\text{theo}})^2 + \sum\limits_{t\in[98,\ 140]} (RF - RF_{\text{theo}})^2}{\text{Number of steps,}}} \tag{10}$$

A controlled random search (CRS) with local mutation (Kaelo and Ali [40]) from the NLOPT library was chosen. More specifically, the lower and upper bounds for [E_c, E_s, k_c, k_s] were respectively set to [10 kPa, 10 kPa, 1×10^{-16} m^2, 1×10^{-16} m^2] and [500 MPa, 500 MPa, 1×10^{-10} m^2, 1×10^{-10} m^2]. Since the parameters' ranges differ from several orders, each parameter was prior normalised with regard to the initial guess to have same order of magnitudes between the optimised unknowns. The initial population size was set to $3 \times (NN + 1)$, where NN is the number of parameters ($NN = 4$ in the present case). This initial population corresponds to random initial points in the search space differing from the input initial guess (15 in the present case). A stopping criterion of 250 evaluations was added, and the optimal solution was kept. Once the calibration was performed, the set of parameters was applied to reproduce the experiment for its complete duration. The algorithm was executed several times, and the result with the lowest RMSE was selected. To ensure convergence, we verified that the material parameters obtained from all calibrations remained within the same order of magnitude, confirming the stability and robustness of the optimization process.

2.7. Initial parameters values

Experimental observations and *in silico* calibration techniques (Khatyr et al. [43], Annaidh et al. [3], Gallagher et al. [24], Ottenio et al. [60], Jacquet et al. [36]) have reported a wide range of values for the Young Modulus ranging from 5 kPa to 196 MPa (Oomens et al. [57]). The models proposing multi-layer analysis, such as the one proposed by Han et al. [30], assume that the cutis is stiffer than the subcutis. This has further been confirmed by the experimental campaigns performed by Connesson et al. [12] and Pailler-Mattei et al. [61]. As a first guess, the Young's moduli were therefore set to $E_c = 1.5 \times 10^6$ Pa and $E_s = 5 \times 10^5$ Pa.

Similarly, a wide domain of values has been reported for the permeability of the medium with values ranging from 1×10^{-16} m^2 to 1×10^{-11} m^2 (Zakaria et al. [91], Swartz and Fleury [77], Levick [47], Oftadeh et al. [52], de Lucio et al. [13], Wahlsten et al. [86]). The initial permeabilities were hence set to $k_c = 1 \times 10^{-14}$ m^2 and $k_s = 1 \times 10^{-13}$ m^2.

Concerning the other material parameters, namely the interstitial fluid viscosity, the Poisson ratio, and the porosity, their value was fixed according to the literature. Sowinski et al. [74] gathered expected viscosity ranges for different human fluids: the cerebrospinal fluid has a viscosity ranging between 0.7-1.0 mPa s, blood between 3.0-67.7 mPa s, ascitic fluid between 0.5-1.5 mPa s. Bera et al. [5] further reported an interstitial fluid dynamic viscosity up to 3.5 mPa s. Swartz and Fleury [77] respectively reported viscosity values for the plasma, lymph, and synovial fluids of 12 mPa s, 15-22 mPa s and 10^2-10^5 mPa s. The authors fixed the interstitial fluid viscosity at $\mu^l = 5$ mPa s. The literature still lacks a clear value of the Poisson ratio, especially for multi-layer models. Therefore, the authors tried to be consistent with values commonly used (Oomens [58], Raveh Tilleman et al. [65], Pailler-Mattei et al. [61], Levy et al. [48]) and assumed a solid scaffold with a compressible behaviour for both phases with a higher Poisson ratio value of the cutis of 0.48 and a more compressible subcutis of 0.3. Finally, Samant and Prausnitz [67] found that the dermis contains approximately 24% of free moving fluid. The hypodermis is thought to be more porous. The values of the porosities for the cutis and subcutis were respectively fixed at 20% and 40%.

The initial guess for the parameters is reported in Table 1.

Cutis Parameters	Initial Value	Unit
Young's modulus (E_c)	1.5×10^5	Pa
Poisson's ratio (ν_c)	0.48	-
Intrinsic permeability (k_c)	4×10^{-14}	m^2
Initial Porosity (ε_c^l)	0.2	-
Subcutis Parameters	Value	Unit
Young's modulus E_s	1×10^5	Pa
Poisson's ratio (ν_s)	0.3	-
Intrinsic permeability (k_s)	3×10^{-13}	m^2
Initial Porosity (ε_s^l)	0.4	-
Fluid phase	Value	Unit
IF viscosity (μ^l)	5×10^{-3}	Pa s

Table 1: Initial mechanical parameters for the bi-compartment model. Italic values refer to the fixed parameters during the calibration procedure.

3. Results

Table 2 provides the calibrated set of parameters. The minimal cost function value was 8.84×10^{-3} N (which corresponds to approximately 2% of the peak reaction force).

Cutis Parameter	Value	Unit
Young modulus (E_c)	684×10^{3}	Pa
Intrinsic permeability (k_c)	9.43×10^{-15}	m^2
Subcutis Parameter	Value	Unit
Young modulus (E_s)	47.8×10^{3}	Pa
Intrinsic permeability (k_s)	5.03×10^{-13}	m^2
Cost Function	Value	Unit
RMSE	8.84×10^{-3}	Pa

Table 2: Calibrated parameters for each layer and optimal cost function value.

The fluid velocity ($\mathbf{v}^l$) is computed all along the simulation from Darcy's law (Equations (11)) to evaluate the fluid displacement within the tissue during the experiment.

$$\mathbf{v}^l = -\frac{k}{\mu\varepsilon}\nabla p + \mathbf{v} \tag{11}$$

Figure 5 shows the evaluated response on the complete experiment. As reflected by the optimal RMSE value, even if a difference in reaction force for negative values is observed and is constant over time (discussed in the next section), the model response allows reproducing the overall behaviour of the reaction force. Especially, it is worth noting that the model was able to recreate the final reflux even though it was not part of the calibration domain. It should be noted that the model provides better predictions for the relaxation phases than the loading and unloading phases.

To obtain insight about the physics, Figure 6 shows the displacement map, the pressure map, and the interstitial fluid flux at different time steps. The authors propose the following interpretation, supporting the time-dependent behaviour of the reaction force from the porous structure. When stretching the skin, it is assumed that the pores get dilated and, therefore, the fluid tends to be drawn in. This was observable on the pressure map through negative values of the interstitial fluid pressure. Conversely, the pores tend to close near the edge of the u-pad and the fluid is expelled which results in a positive interstitial pressure.

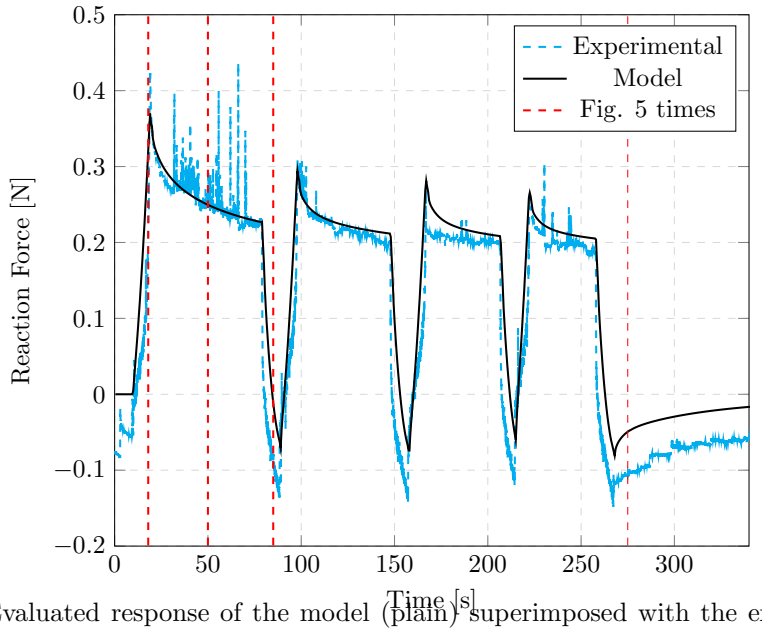

Figure 5: Evaluated response of the model (plain) superimposed with the experimental reaction force (dashed) for all the cycles. The model was able to reproduce the reaction force for the four cycles of the experiment. The vertical dashed lines represent the time steps shown in Figure 6.

During a sustained phase, the tissue tends to slowly recover its homeostatic state. When releasing the tissue, a strong reflux occurs with high positive pressure values: the fluid retrieves its initial place. Finally, the last reflux slowly comes back to a homogenised pressure state within the tissue.

It is furthermore worth noting that, due to a lower value of the permeability in the cutis phase, most of the fluid flow is concentrated in the subcutis for all the phases.

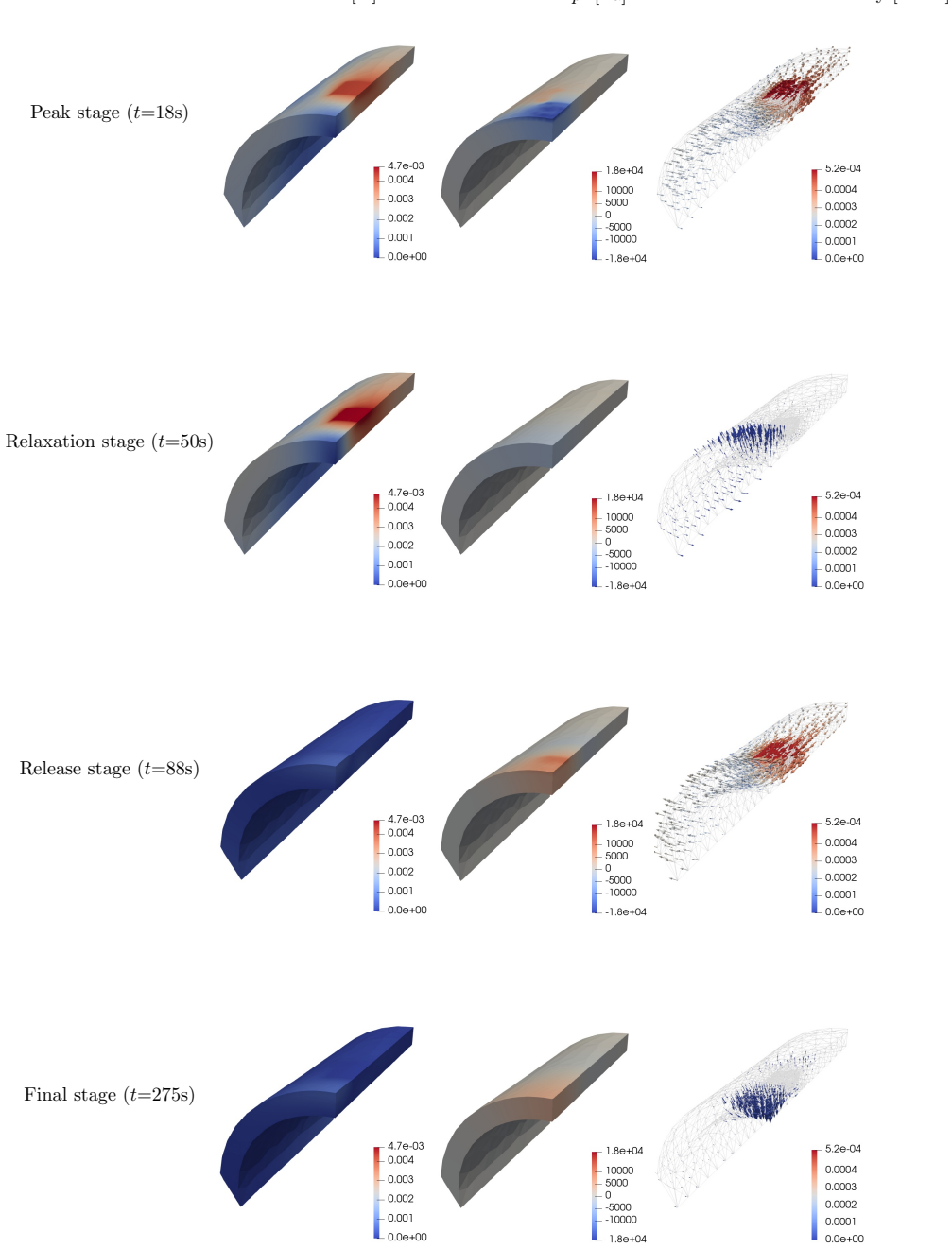

Figure 6: From left to right: displacement magnitude, interstitial fluid pressure, interstitial fluid velocity maps. The results represent the maximum load time ($t = 18$ s), a sustained phase ($t = 50$ s), a relaxed phase ($t = 88$ s) and the final reflux ($t = 275$ s). When stretching the skin, the fluid tends to be drawn in, resulting in negative values of the interstitial fluid pressure. Conversely, the pores tend to close near to the edge of the u-pad and the fluid is expelled which results in a positive interstitial pressure. During a sustained phase, stabilises towards its homeostatic state. When releasing the tissue, a reflux occurs. The fluid flow images are further included in Appendix B for the ease of the reading. A description of the fluid movement is further introduced.

4. Discussion

Motivated by the limited *in vivo* application of biphasic constitutive modelling for parameter identification, a poro-hyper-elastic model has been implemented in the FEniCSx environment and calibrated to reproduce the time-dependent mechanical response of upper-arm skin under cyclic uni-axial extension including the final reflux phase. The Root Mean Square Error between the calibrated model and the measured Force-time response was 8.84×10^{-3} N. The calibrated parameters align with previously reported values, confirming that the subcutis is softer than the cutis (section 2.7). The Young's modulus of the cutis ($E_c = 684$ kPa) maintains the body geometry, being almost 10 times stiffer than the subcutis. Specifically, the Young's modulus of the cutis ($E_c = 684$kPa) functions to absorb external mechanical loads. Interstitial fluid presence contributes to load cushioning and sustains the time-dependent mechanical response. A single fluid compartment was considered for each layer, and permeability was calibrated to reflect interstitial fluid movement. The cutis' intrinsic permeability is 9.43×10^{-15} m^2, while the subcutis permeability is 50 times higher at 5.03×10^{-13} m^2. As a result, the pressure distribution observed in Figure 6, especially at the corners differs between the cutis and the subcutis. The pressure magnitude is higher in the cutis, and this is due to the heterogeneity in permeability across layers: a smaller permeability results in a higher pressure value.

However, this study has limitations. The first one is related to the noise from the sensors which were firstly designed for keloids (Chambert et al. [11]), which are stiffer than healthy skin. Furthermore, the authors recognise that the current study is based on a single mechanical trial conducted on one subject, serving as an initial investigation to validate the proposed approach. To strengthen the robustness of the findings, future research will involve an expanded sample size and additional trials. Specifically, this patient presented a keloid on her right upper arm and this experimental data was acquired on the other arm to compare the mechanical properties between the keloid-affected area and the healthy skin. This experimental data had not been utilised further and thus provided an opportunity for evaluating the model. Despite this, the study demonstrates the poro-hyper-elastic model's *in vivo* performance in loading-sustaining-unloading tests, providing valuable insights into the dissipative effect of human skin. It is however difficult to distinguish between viscoelastic and poroelastic dissipation when only limited boundary condition information is known. Future experimental

campaigns should consider testing different strain rates to evaluate the viscoelastic contribution in the mechanical response. Likewise, the permeability values obtained in this article should be understand with a high uncertainty, as their sensitivities are low (see Appendix) and the range of values reported in the literature is wide.

Furthermore, a difference is observed for negative values of the reaction force. We believe that the negative forces are likely due to prestress introduced when the experimental device is glued to the skin. This prestress could arise from the initial tension or deformation caused by the adhesive bond between the device and the skin. However, no pre-stress was introduced and the gap in force is constant for all the minimal values. Overlooking the pre-stress - which may impact the results of a hyper-elastic formulation, the authors however chose not to set to zero the first values to limit misinterpretation of the results. This might impact the Young modulus value, but the global conclusions are not expected to change.

Only two layers were considered in the model: the cutis and the subcutis, similar to the approach taken by Connesson et al. [12]. The cutis, however, can be further subdivided into the epidermis and dermis, with the epidermis primarily composed of cells and the dermis consisting of cells embedded in an extracellular matrix. Given the thickness of each layer and the scale of the geometry under consideration, modelling them as separate layers would significantly increase the number of elements in the mesh, thereby raising the computational cost. This supports the decision to combine them into a single layer. Future studies could explore the subdivision of this layer and investigate its impact on the mechanical response. Integrating ANN-based techniques with our model could help improving computational efficiency and allow for this more detailed multiscale description (Dehghani and Zilian [14]). Furthermore, the interaction between cutis and subcutis is handled through differing material properties rather than explicit displacement/stress boundary conditions. We acknowledge that this creates a lower-fidelity bilayered model but avoids introducing a new unknown in the problem (*e.g.* friction coefficient). Future study could focus on measuring the relative displacement between the layers during extension tests.

Additionally, the skin was stretched up to 25 %. As shown in Figure 6, while the subcutis layer follows the cutis, the deformation is not uniform throughout its depth; the extension test causes deformation that extends into the subcutis layer. Due to a lack of experimental data, no adherence was modelled at the bottom of the subcutis, but this effect might be more

pronounced if adherence were considered, potentially increasing shear within the tissue.

The model assumes isotropy due to the limited data available along other directions, as the experiment only provided measurements of axial force and displacement. However, the skin's fibrous nature suggests at least transversely isotropic behaviour, as supported by previous studies Khatyr et al. [43], Annaidh et al. [3], Kalra and Lowe [41], Joodaki and Panzer [39], Yazdi and Baqersad [90], Elouneg et al. [18]. This assumption has implications for the results, as the model may not accurately capture the skin's behaviour in directions where significant anisotropy is expected—such as along the skin's fibres or in response to differential fluid flow.

Future work should focus on extending the model to account for anisotropy by incorporating directional dependencies in the material parameters. Specifically, material properties should vary based on the direction of preferred fluid flow and the orientation of the collagen-elastin fibres in the skin. Additionally, imaging techniques should be integrated to enhance parameter identification and improve the accuracy of the model.

Moreover, the selection of a more suitable hyper-elastic potential should be explored to better capture the mechanical response non-linearity during both the loading and unloading phases. Further developments could also include the introduction of a viscous transverse hyper-elastic phase, which would better accommodate the fast time constants observed in the system.

Porous media models represent a promising approach for integrating multiscale/multiphysics data to probe biologically relevant phenomena at smaller scales and embed relevant mechanisms at larger scales. This is particularly the case with regard to the interaction of multiple biochemical factors (enzymes, growth factors, hormones, proteins) and the complex network of regulatory signals, which determine tissue characteristics and their evolution in processes such as growth and remodelling (Eskandari and Kuhl [21]), ageing, and the onset of injuries such as pressure ulcers (Sree et al. [75], Gefen et al. [25]).

The model, tested against the *in vivo* data, shows promise, particularly in understanding tissue necrosis, pressure ulcer onsets, and prevention. Indeed, the aetiology of Pressure Ulcers (PUs) showed that multiple factors lead to the onset of such complications. Especially, a (PU) is assumed to result both from excessive loading and ischaemic damage, which occur at different time and length scales (Loerakker et al. [49]). Coupling with a second compartment, representative of microvasculature, could offer insights into biochemical

and mechanical reactions during mechanical load application (Sciumè et al. [70], Kremheller et al. [44], Urcun et al. [82, 80]).

The encouraging results obtained in this preliminary work allow for the analysis of changes in IF pressure and flow and osmotic pressure, in addition to the mechanical fields. It represents a first step towards investigating the mechanical conditions responsible for tissue characteristics and their evolution in processes such as growth and remodelling, ageing, and the onset of injuries such as pressure ulcers, this preliminary study focused on applying poromechanical models. More specifically, the proposed modelling approach potentially can pave the way for a better understanding of fibrosis phenomena such as keloid disorders by taking into account the time-dependent mechanical behaviour, which is not the case in recent literature (Sutula et al. [76], Elouneg et al. [19], Elouneg [17]).

5. Conclusion

This paper aimed to evaluate a poromechanical model to reproduce unpublished data collected on *in vivo* human skin during extension tests. A complete framework to identify the time-dependent properties of the skin was introduced within the Open-Source environment FEniCSx. The calibration was performed on the first cycles of the experiment. The complete experiment was computed afterwards to evaluate the predictability capacity of the model. A good agreement has been found between the numerical and experimental responses. Furthermore, the identified mechanical parameters are relevant with the literature. This study therefore supports the use of a poro-mechanical model for the skin under extension testing. More experiments are however required with, for the IF phase, a better control on the boundary conditions and a better monitoring during the experiment. This would allow to distinguish between viscoelastic and poroelastic dissipation.

Acknowledgments

This research was funded in whole, or in part, by the Luxembourg National Research Fund (FNR), grant reference No. 17013182. For the purpose of open access, the author has applied a Creative Commons Attribution 4.0 International (CC BY 4.0) license to any Author Accepted Manuscript version arising from this submission. The present project is also supported by the National Research Fund, Luxembourg, under grant No. C20/MS/14782078/QuaC

and the French National Research Fund (ANR) under grant No. ANR-21-CE45-0025 for the project S-KELOID. The experimental part of this work has been achieved in the frame of the EIPHI Graduate school (contract "ANR-17-EURE-0002")

Declarations

Competing interests: The authors declare that they have no known competing financial interests or personal relationships that could have appeared to influence the work reported in this paper.

Supplementary material: The python codes corresponding to the FEniCSx models and the experimental data of this article are made available on the following link: `https://github.com/Th0masLavigne/Skin_porous_modelling.git`.

References

[1] Agache, P. G., Monneur, C., Leveque, J. L., and De Rigal, J. (1980). Mechanical properties and Young's modulus of human skin in vivo. *Archives of Dermatological Research*, 269:221–232.

[2] Alexander, H. and Cook, T. (1977). Accounting for natural tension in the mechanical testing of human skin. *Journal of Investigative Dermatology*, 69(3):310–314.

[3] Annaidh, A. N., Bruyère, K., Destrade, M., Gilchrist, M. D., and Otténio, M. (2012). Characterization of the anisotropic mechanical properties of excised human skin. *Journal of the Mechanical Behavior of Biomedical Materials*, 5(1):139–148.

[4] Argoubi, M. and Shirazi-Adl, A. (1996). Poroelastic creep response analysis of a lumbar motion segment in compression. *Journal of Biomechanics*, 29(10):1331–1339.

[5] Bera, K., Kiepas, A., Godet, I., Li, Y., Mehta, P., Ifemembi, B., Paul, C. D., Sen, A., Serra, S. A., Stoletov, K., Tao, J., Shatkin, G., Lee, S. J., Zhang, Y., Boen, A., Mistriotis, P., Gilkes, D. M., Lewis, J. D., Fan, C.-M., Feinberg, A. P., Valverde, M. A., Sun, S. X., and Konstantopoulos, K. (2022). Extracellular fluid viscosity enhances cell migration and cancer dissemination. *Nature*, 611(7935):365–373.

[6] Birkebaek, N., Johansen, A., and Solvig, J. (1998). Cutis/subcutis thickness at insulin injection sites and localization of simulated insulin boluses in children with type 1 diabetes mellitus: need for individualization of injection technique? *Diabetic Medicine*, 15(11):965–971.

[7] Bosboom, E., Hesselink, M., Oomens, C., Bouten, C., Drost, M., and Baaijens, F. (2001). Passive transverse mechanical properties of skeletal muscle under in vivo compression. *Journal of Biomechanics*, 34(10):1365–1368.

[8] Budday, S., Ovaert, T. C., Holzapfel, G. A., Steinmann, P., and Kuhl, E. (2019). Fifty shades of brain: A review on the mechanical testing and modeling of brain tissue. *Archives of Computational Methods in Engineering*, 27(4):1187–1230.

[9] Bulle, R. (2022). *A posteriori error estimation for finite element approximations of fractional Laplacian problems and applications to poroelasticity*. Theses, Université Bourgogne Franche-Comté ; Université du Luxembourg.

[10] Carrasco-Mantis, A., Randelovic, T., Castro-Abril, H., Ochoa, I., Doblaré, M., and Sanz-Herrera, J. A. (2023). A mechanobiological model for tumor spheroid evolution with application to glioblastoma: A continuum multiphysics approach. *Computers in Biology and Medicine*, 159:106897.

[11] Chambert, J., Lihoreau, T., Joly, S., Chatelain, B., Sandoz, P., Humbert, P., Jacquet, E., and Rolin, G. (2019). Multimodal investigation of a keloid scar by combining mechanical tests in vivo with diverse imaging techniques. *Journal of the Mechanical Behavior of Biomedical Materials*, 99:206–215.

[12] Connesson, N., Briot, N., Rohan, P. Y., Barraud, P. A., Elahi, S. A., and Payan, Y. (2023). Bilayer stiffness identification of soft tissues by suction. *Experimental Mechanics*, 63(4):715–742.

[13] de Lucio, M., Leng, Y., Hans, A., Bilionis, I., Brindise, M., Ardekani, A. M., Vlachos, P. P., and Gomez, H. (2023). Modeling large-volume subcutaneous injection of monoclonal antibodies with anisotropic porohyperelastic models and data-driven tissue layer geometries. *Journal of the Mechanical Behavior of Biomedical Materials*, 138:105602.

[14] Dehghani, H. and Zilian, A. (2023). Finite strain poro-hyperelasticity: an asymptotic multi-scale ale-fsi approach supported by anns. *Computational Mechanics*, 71(4):695–719.

[15] Doll, S. and Schweizerhof, K. (2000). On the development of volumetric strain energy functions. *Journal of Applied Mechanics*, 67(1):17–21.

[16] Dubois, A., Levecq, O., Azimani, H., Siret, D., Barut, A., Suppa, M., del Marmol, V., Malvehy, J., Cinotti, E., Rubegni, P., and Perrot, J.-L. (2018). Line-field confocal optical coherence tomography for high-resolution noninvasive imaging of skin tumors. *Journal of Biomedical Optics*, 23(10):106007.

[17] Elouneg, A. (2023). *In vivo mechanical characterization of soft tissues : application to human skin and keloid*. Theses, Université Bourgogne Franche-Comté ; Université du Luxembourg.

[18] Elouneg, A., Chambert, J., Lejeune, A., Lucot, Q., Jacquet, E., and Bordas, S. (2023). Anisotropic mechanical characterization of human skin by in vivo multi-axial ring suction test. *Journal of the Mechanical Behavior of Biomedical Materials*, 141:105779.

[19] Elouneg, A., Sutula, D., Chambert, J., Lejeune, A., Bordas, S., and Jacquet, E. (2021). An open-source fenics-based framework for hyperelastic parameter estimation from noisy full-field data: Application to heterogeneous soft tissues. *Computers & Structures*, 255:106620.

[20] Eshel, H. and Lanir, Y. (2001). Effects of strain level and proteoglycan depletion on preconditioning and viscoelastic responses of rat dorsal skin. *Annals of Biomedical Engineering*, 29(2):164–172.

[21] Eskandari, M. and Kuhl, E. (2015). Systems biology and mechanics of growth. *Wiley Interdiscip. Rev. Syst. Biol. Med.*, 7(6):401–412.

[22] Flynn, C., Taberner, A., and Nielsen, P. (2010). Mechanical characterisation of in vivo human skin using a 3d force-sensitive micro-robot and finite element analysis. *Biomechanics and Modeling in Mechanobiology*, 10(1):27–38.

[23] Franceschini, G., Bigoni, D., Regitnig, P., and Holzapfel, G. (2006). Brain tissue deforms similarly to filled elastomers and follows consolidation theory. *Journal of the Mechanics and Physics of Solids*, 54(12):2592–2620.

[24] Gallagher, A., Ní Annaidh, A., Bruyère, K., Otténio, M., Xie, H., and Gilchrist, M. (2012). Dynamic tensile properties of human skin. In *IRCOBI conference*, volume 59, pages 494–502. International Research Council on the Biomechanics of Injury Dublin (Ireland.

[25] Gefen, A., Brienza, D. M., Cuddigan, J., Haesler, E., and Kottner, J. (2022). Our contemporary understanding of the aetiology of pressure ulcers/pressure injuries. *Int. Wound J.*, 19(3):692–704.

[26] Gerhardt, L.-C., Schmidt, J., Sanz-Herrera, J., Baaijens, F., Ansari, T., Peters, G., and Oomens, C. (2012). A novel method for visualising and quantifying through-plane skin layer deformations. *Journal of the Mechanical Behavior of Biomedical Materials*, 14:199–207.

[27] Geuzaine, C. and Remacle, J.-F. (2018). Gmsh.

[28] Gimnich, O. A., Singh, J., Bismuth, J., Shah, D. J., and Brunner, G. (2019). Magnetic resonance imaging based modeling of microvascular perfusion in patients with peripheral artery disease. *Journal of Biomechanics*, 93:147–158.

[29] Greiner, A., Reiter, N., Paulsen, F., Holzapfel, G. A., Steinmann, P., Comellas, E., and Budday, S. (2021). Poro-viscoelastic effects during biomechanical testing of human brain tissue. *Frontiers in Mechanical Engineering*, 7.

[30] Han, D., Huang, Z., Rahimi, E., and Ardekani, A. M. (2023). Solute transport across the lymphatic vasculature in a soft skin tissue. *Biology*, 12(7):942.

[31] Hargens, A. R., Cologne, J. B., Menninger, F. J., Hogan, J. S., Tucker, B. J., and Peters, R. M. (1981). Normal transcapillary pressures in human skeletal muscle and subcutaneous tissues. *Microvascular research*, 22(2):177–189.

[32] Hervas-Raluy, S., Wirthl, B., Guerrero, P. E., Robalo Rei, G., Nitzler, J., Coronado, E., Font de Mora Sainz, J., Schrefler, B. A., Gomez-Benito, M. J., Garcia-Aznar, J. M., and Wall, W. A. (2023). Tumour growth: An approach to calibrate parameters of a multiphase porous media model based on in vitro observations of neuroblastoma spheroid growth in a hydrogel microenvironment. *Computers in Biology and Medicine*, 159:106895.

[33] Horgan, C. O. and Saccomandi, G. (2004). Constitutive models for compressible nonlinearly elastic materials with limiting chain extensibility. *Journal of Elasticity*, 77(2):123–138.

[34] Hosseini-Farid, M., Ramzanpour, M., McLean, J., Ziejewski, M., and Karami, G. (2020). A poro-hyper-viscoelastic rate-dependent constitutive modeling for the analysis of brain tissues. *Journal of the Mechanical Behavior of Biomedical Materials*, 102:103475.

[35] Humbert, P., Fanian, F., Maibach, H. I., and Agache, P., editors (2017). *Agache's Measuring the Skin – Non-invasive Investigations, Physiology, Normal Constants*. Springer International Publishing, Switzerland, Second edition.

[36] Jacquet, E., Chambert, J., Pauchot, J., and Sandoz, P. (2017a). Intra- and inter-individual variability in the mechanical properties of the human skin from in vivo measurements on 20 volunteers. *Skin Research and Technology*, 23(4):491–499.

[37] Jacquet, E., Joly, S., Chambert, J., Rekik, K., and Sandoz, P. (2017b). Ultra-light extensometer for the assessment of the mechanical properties of the human skin in vivo. *Skin Research and Technology*, 23(4):531–538.

[38] Jasaitiene, D., Valiukeviciene, S., Linkeviciute, G., Raisutis, R., Jasiuniene, E., and Kazys, R. (2011). Principles of high-frequency ultrasonography for investigation of skin pathology. *Journal of the European Academy of Dermatology and Venereology*, 25(4):375–382.

[39] Joodaki, H. and Panzer, M. B. (2018). Skin mechanical properties and modeling: A review. *Proceedings of the Institution of Mechanical Engineers, Part H: Journal of Engineering in Medicine*, 232(4):323–343.

[40] Kaelo, P. and Ali, M. M. (2006). Some variants of the controlled random search algorithm for global optimization. *Journal of Optimization Theory and Applications*, 130(2):253–264.

[41] Kalra, A. and Lowe, A. (2016). Mechanical behaviour of skin: A review. *Journal of Material Science & Engineering*, 5(4).

[42] Kazemi, M., Dabiri, Y., and Li, L. P. (2013). Recent advances in computational mechanics of the human knee joint. *Computational and Mathematical Methods in Medicine*, 2013:1–27.

[43] Khatyr, F., Imberdis, C., Vescovo, P., Varchon, D., and Lagarde, J.-M. (2004). Model of the viscoelastic behaviour of skin in vivo and study of anisotropy. *Skin Research and Technology*, 10(2):96–103.

[44] Kremheller, J., Vuong, A., Schrefler, B. A., and Wall, W. A. (2019). An approach for vascular tumor growth based on a hybrid embedded/homogenized treatment of the vasculature within a multiphase porous medium model. *International Journal for Numerical Methods in Biomedical Engineering*, 35(11).

[45] Lavigne, T., Sciumè, G., Laporte, S., Pillet, H., Urcun, S., Wheatley, B., and Rohan, P.-Y. (2022). Société de biomécanique young investigator award 2021: Numerical investigation of the time-dependent stress–strain mechanical behaviour of skeletal muscle tissue in the context of pressure ulcer prevention. *Clinical Biomechanics*, 93:105592.

[46] Lavigne, T., Urcun, S., Rohan, P.-Y., Sciumè, G., Baroli, D., and Bordas, S. P. (2023). Single and bi-compartment poro-elastic model of perfused biological soft tissues: FEniCSx implementation and tutorial. *Journal of the Mechanical Behavior of Biomedical Materials*, 143:105902.

[47] Levick, J. R. (1987). Flow through interstitium and other fibrous matrices. *Quarterly Journal of Experimental Physiology*, 72(4):409–437.

[48] Levy, A., Frank, M. B.-O., and Gefen, A. (2015). The biomechanical efficacy of dressings in preventing heel ulcers. *Journal of Tissue Viability*, 24(1):1–11.

[49] Loerakker, S., Manders, E., Strijkers, G. J., Nicolay, K., Baaijens, F. P. T., Bader, D. L., and Oomens, C. W. J. (2011). The effects of deformation, ischemia, and reperfusion on the development of muscle damage during prolonged loading. *Journal of Applied Physiology*, 111(4):1168–1177.

[50] Marino, M. (2018). *Constitutive Modeling of Soft Tissues*, page 81–110. Elsevier.

[51] Mellor, R. H., Bush, N. L., Stanton, A. W. B., Bamber, J. C., Levick, J. R., and Mortimer, P. S. (2004). Dual-frequency ultrasound examination of skin and subcutis thickness in breast cancer-related lymphedema. *The Breast Journal*, 10(6):496–503.

[52] Oftadeh, R., Connizzo, B. K., Nia, H. T., Ortiz, C., and Grodzinsky, A. J. (2018). Biological connective tissues exhibit viscoelastic and poroelastic behavior at different frequency regimes: Application to tendon and skin biophysics. *Acta Biomaterialia*, 70:249–259.

[53] Ogawa, R., Okai, K., Tokumura, F., Mori, K., Ohmori, Y., Huang, C., Hyakusoku, H., and Akaishi, S. (2012). The relationship between skin stretching/contraction and pathologic scarring: the important role of mechanical forces in keloid generation. *Wound Repair and Regeneration*, 20(2):149–157.

[54] Oomens, C., van Campen, D., and Grootenboer, H. (1987a). In vitro compression of a soft tissue layer on a rigid foundation. *Journal of Biomechanics*, 20(10):923–935.

[55] Oomens, C., van Campen, D., and Grootenboer, H. (1987b). A mixture approach to the mechanics of skin. *Journal of Biomechanics*, 20(9):877–885.

[56] Oomens, C., van Campen, D., and Grootenboer, H. (1987c). A mixture approach to the mechanics of skin. *Journal of Biomechanics*, 20(9):877–885.

[57] Oomens, C. W., van Vijven, M., and Peters, G. W. (2017). Chapter 16 - skin mechanics. In Payan, Y. and Ohayon, J., editors, *Biomechanics of Living Organs*, volume 1 of *Translational Epigenetics*, pages 347–357. Academic Press, Oxford.

[58] Oomens, C. W. J. (1985). A mixture approach to the mechanics of skin and subcutis: a contribution to pressure sore research. *Journal of biomechanics*.

[59] Oomens, C. W. J., Van Campen, D. H., Grootenboer, H. J., and De Boer, L. J. (1985). *Experimental and Theoretical Compression Studies on Porcine Skin*, page 227–232. Springer Netherlands.

[60] Ottenio, M., Tran, D., Annaidh, A. N., Gilchrist, M. D., and Bruyère, K. (2015). Strain rate and anisotropy effects on the tensile failure characteristics of human skin. *Journal of the Mechanical Behavior of Biomedical Materials*, 41:241–250.

[61] Pailler-Mattei, C., Bec, S., and Zahouani, H. (2008). In vivo measurements of the elastic mechanical properties of human skin by indentation tests. *Medical Engineering & Physics*, 30(5):599–606.

[62] Pailler-Mattéi, C. and Zahouani, H. (2004). Study of adhesion forces and mechanical properties of human skin in vivo. *Journal of Adhesion Science and Technology*, 18(15–16):1739–1758.

[63] Pence, T. J. and Gou, K. (2014). On compressible versions of the incompressible neo-hookean material. *Mathematics and Mechanics of Solids*, 20(2):157–182.

[64] Peyrounette, M., Davit, Y., Quintard, M., and Lorthois, S. (2018). Multiscale modelling of blood flow in cerebral microcirculation: Details at capillary scale control accuracy at the level of the cortex. *PLOS ONE*, 13(1):e0189474.

[65] Raveh Tilleman, T., Tilleman, M., and Neumann, H. (2004). The elastic properties of cancerous skin: Poisson's ratio and young's modulus. *Optimization of Incisions in Cutaneous Surgery including Mohs' Micrographic Surgery*, 105(2).

[66] Ricken, T. and Lambers, L. (2019). On computational approaches of liver lobule function and perfusion simulation. *GAMM-Mitteilungen*, 42(4).

[67] Samant, P. P. and Prausnitz, M. R. (2018). Mechanisms of sampling interstitial fluid from skin using a microneedle patch. *Proceedings of the National Academy of Sciences*, 115(18):4583–4588.

[68] Sciumè, G. (2021). Mechanistic modeling of vascular tumor growth: an extension of biot's theory to hierarchical bi-compartment porous medium systems. *Acta Mechanica*, 232(4):1445–1478.

[69] Sciumè, G., Boso, D. P., Gray, W. G., Cobelli, C., and Schrefler, B. A. (2014). A two-phase model of plantar tissue: a step toward prediction of diabetic foot ulceration. *International Journal for Numerical Methods in Biomedical Engineering*, 30(11):1153–1169.

[70] Sciumè, G., Gray, W. G., Hussain, F., Ferrari, M., Decuzzi, P., and Schrefler, B. A. (2013). Three phase flow dynamics in tumor growth. *Computational Mechanics*, 53(3):465–484.

[71] Shergold, O. A., Fleck, N. A., and Radford, D. (2006). The uniaxial stress versus strain response of pig skin and silicone rubber at low and high strain rates. *International Journal of Impact Engineering*, 32(9):1384–1402.

[72] Siddique, J., Ahmed, A., Aziz, A., and Khalique, C. (2017). A review of mixture theory for deformable porous media and applications. *Applied Sciences*, 7(9):917.

[73] Simo, J. (1988). A framework for finite strain elastoplasticity based on maximum plastic dissipation and the multiplicative decomposition: Part i. continuum formulation. *Computer Methods in Applied Mechanics and Engineering*, 66(2):199–219.

[74] Sowinski, D. R., McGarry, M. D. J., Houten, E. E. W. V., Gordon-Wylie, S., Weaver, J. B., and Paulsen, K. D. (2021). Poroelasticity as a model of soft tissue structure: Hydraulic permeability reconstruction for magnetic resonance elastography in silico. *Frontiers in Physics*, 8.

[75] Sree, V. D., Rausch, M. K., and Tepole, A. B. (2019). Linking microvascular collapse to tissue hypoxia in a multiscale model of pressure ulcer initiation. *Biomech. Model. Mechanobiol.*, 18(6):1947–1964.

[76] Sutula, D., Elouneg, A., Sensale, M., Chouly, F., Chambert, J., Lejeune, A., Baroli, D., Hauseux, P., Bordas, S., and Jacquet, E. (2020). An open source pipeline for design of experiments for hyperelastic models of the skin with applications to keloids. *Journal of the Mechanical Behavior of Biomedical Materials*, 112:103999.

[77] Swartz, M. A. and Fleury, M. E. (2007). Interstitial flow and its effects in soft tissues. *Annual Review of Biomedical Engineering*, 9(1):229–256.

[78] Tong, P. and Fung, Y.-C. (1976). The stress-strain relationship for the skin. *Journal of Biomechanics*, 9(10):649–657.

[79] Tran, H. (2007). *Caractérisation des propriétés mécaniques de la peau humaine in vivo via l'IRM*. Theses, Université de Technologie de Compiègne.

[80] Urcun, S., Baroli, D., Rohan, P.-Y., Skalli, W., Lubrano, V., Bordas, S. P., and Sciume, G. (2023). Non-operable glioblastoma: proposition of patient-specific forecasting by image-informed poromechanical model. *Brain Multiphysics*, page 100067.

[81] Urcun, S., Rohan, P.-Y., Sciumè, G., and Bordas, S. P. (2022). Cortex tissue relaxation and slow to medium load rates dependency can be captured by a two-phase flow poroelastic model. *Journal of the Mechanical Behavior of Biomedical Materials*, 126:104952.

[82] Urcun, S., Rohan, P.-Y., Skalli, W., Nassoy, P., Bordas, S. P. A., and Sciumè, G. (2021). Digital twinning of cellular capsule technology: Emerging outcomes from the perspective of porous media mechanics. *PLOS ONE*, 16(7):e0254512.

[83] Uzuner, S., Kuntze, G., Li, L., Ronsky, J., and Kucuk, S. (2022). Creep behavior of human knee joint determined with high-speed biplanar videoradiography and finite element simulation. *Journal of the Mechanical Behavior of Biomedical Materials*, 125:104905.

[84] Uzuner, S., Li, L., Kucuk, S., and Memisoglu, K. (2020). Changes in knee joint mechanics after medial meniscectomy determined with a poromechanical model. *Journal of Biomechanical Engineering*, 142(10).

[85] Waghule, T., Singhvi, G., Dubey, S. K., Pandey, M. M., Gupta, G., Singh, M., and Dua, K. (2019). Microneedles: A smart approach and increasing potential for transdermal drug delivery system. *Biomedicine & pharmacotherapy*, 109:1249–1258.

[86] Wahlsten, A., Pensalfini, M., Stracuzzi, A., Restivo, G., Hopf, R., and Mazza, E. (2019). On the compressibility and poroelasticity of human and murine skin. *Biomechanics and Modeling in Mechanobiology*, 18(4):1079–1093.

[87] Wahlsten, A., Stracuzzi, A., Lüchtefeld, I., Restivo, G., Lindenblatt, N., Giampietro, C., Ehret, A. E., and Mazza, E. (2023). Multiscale mechanical analysis of the elastic modulus of skin. *Acta Biomater.*, 170:155–168.

[88] Weir Weiss, M.-J., Shrestha, P., Basak, R., and Stoeber, B. (2023). Poroelastic behavior of skin tissue in response to pressure driven flow. *Physics of Fluids*, 35(8):081902.

[89] Wiig, H. and Noddeland, H. (1983). Interstitial fluid pressure in human skin measured by micropuncture and wick-in-needle. *Scandinavian Journal of Clinical and Laboratory Investigation*, 43(3):255–260.

[90] Yazdi, S. J. M. and Baqersad, J. (2022). Mechanical modeling and characterization of human skin: A review. *Journal of Biomechanics*, 130:110864.

[91] Zakaria, E. R., Lofthouse, J., and Flessner, M. F. (1997). In vivo hydraulic conductivity of muscle: effects of hydrostatic pressure. *American Journal of Physiology-Heart and Circulatory Physiology*, 273(6):H2774–H2782.

[92] Zhang, M., Turner-Smith, A. R., and Roberts, V. C. (1994). The reaction of skin and soft tissue to shear forces applied externally to the skin surface. *Proceedings of the Institution of Mechanical Engineers, Part H: Journal of Engineering in Medicine*, 208(4):217–222.

Appendix A. Sobol' indices

Sobol' indices were computed for the poromechanical material parameters and the initial IF pressure. More precisely, a 'reference' evaluation was computed and the reaction force was recorded. Each parameter was then moved by 10% forward and backward, and the resulting reaction force was saved.

The error metric defined to evaluate the impact of the parameter is the mean of the relative difference of the reaction force between 18 s and 50 s. The

slope of the curve between the error metrics (θ_i) is then computed for each parameter, and the Sobol' indices are estimated as $S_i = \frac{\theta_i^2}{\sum \theta_i^2}$. The parameters accounting for 90% of the variance are considered for the calibration.

	θ_i	S_i
E_c	28.7	5.27×10^{-1}
E_s	25.4	4.12×10^{-1}
ε_c	-2.44×10^{-5}	3.80×10^{-13}
ε_s	-2.06×10^{-4}	2.71×10^{-11}
k_c	-1.6×10^{-1}	1.64×10^{-5}
k_s	-9.71	6.02×10^{-2}
p_{init}	-1.09×10^{-4}	7.63×10^{-12}

Table A.3: Sobol indices of the model's parameters.

According to Table A.3, the governing parameters are the Young moduli and the permeability of the subcutis. The permeability of the cutis was added to the calibrated parameters to complete the set of guesses.

Appendix B. Interstitial Fluid flow

$t = 18\,\mathrm{s}$

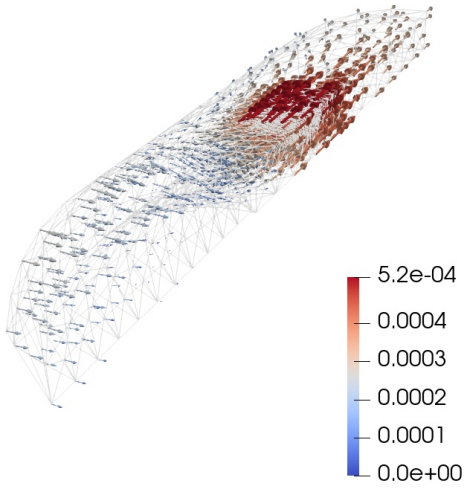

$t = 50\,\mathrm{s}$

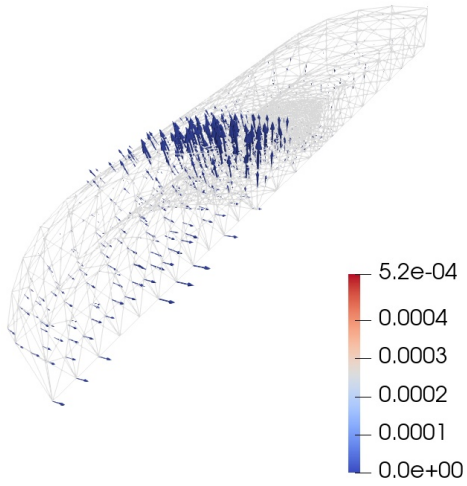

$t = 88\,\mathrm{s}$

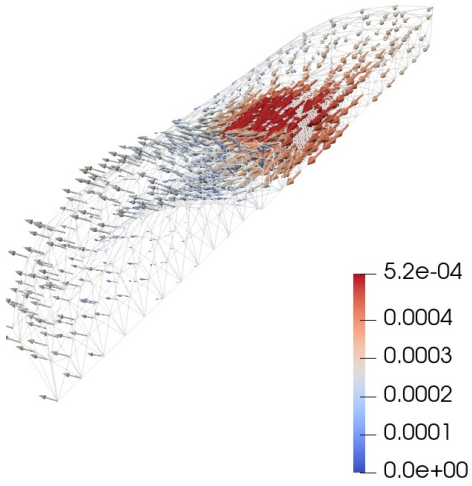

$t = 275\,\mathrm{s}$

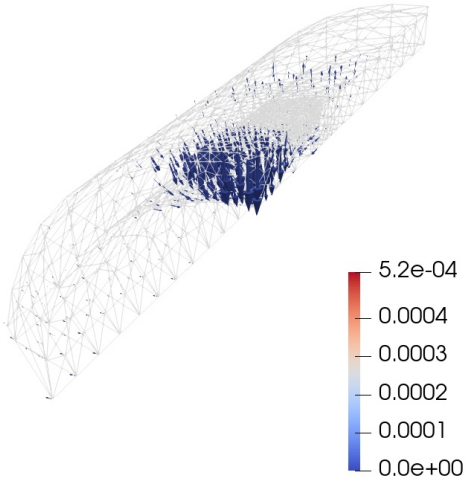

When stretching the skin, the fluid underneath the patch slowly follows the patch movements and the neighbouring fluid is drawn in the pores which get dilated (peak at t=18s). During a sustained phase (t=50s), an equilibrium phase is reached and the fluid moves from the subcutis to the cutis. Then, during a release phase (t=88s), the fluid is expelled from the deformed region to be replaced by the one underneath the patch. Finally, during the last stage (t=275s), the initial state is reached again and a movement of fluid from the cutis to the subcutis is expected.